ELSEVIER

International Journal of Mass Spectrometry 208 (2001) 227–242

International Journal of Mass Spectrometry

Isotopic ratio measurements by time-of-flight secondary ion mass spectrometry

A.J. Fahey,* S. Messenger

Chemical Science and Technology Laboratory, National Institute of Standards and Technology, 100 Bureau Drive, Stop 8371, B/222 R/A 113, Gaithersburg, MD, USA

Received 13 July 2000; accepted 30 March 2001

Abstract

Time-of-Flight Secondary Ion Mass Spectrometry (ToF–SIMS) is often considered synonymous with SIMS in the static limit where the ion fluence on the sample surface is so low that damage is negligible. For this same reason, its use in measuring isotopic ratios has generally been ruled out. However, the high-spatial-resolution Ga^+ ion beams typically used in ToF–SIMS make it a potentially attractive technique for the isotopic characterization of small features such as particles. We have developed a technique to measure isotopic ratios by ToF–SIMS with a spatial resolution of <1 μm. Peak-fitting and interference-stripping algorithms have been developed and are presented in this work. The precision of the measurements is close to counting statistical limits, and the variability in mass bias is comparable to dynamic SIMS. (Int J Mass Spectrom 208 (2001) 227–242) © 2001 Elsevier Science B.V.

Key words: Isotopic ratio measurements; ToF–SIMS; SIMS

1. Introduction

Isotopic ratio measurements have been made in ToF mass spectrometers by several investigators (e.g., Ti isotopes with a laser desorption/RIMS instrument [1]) with good results. Dead-time corrections have been investigated and applied to the measurement of Ag isotopes and for image correction [2]. However, isotope ratio measurements by ToF–SIMS have not been extensively investigated and have not been applied to the determination of small-particle compositions. Isotopic measurements of elements such as Si, Mg, and Ti require high mass resolution so that interferences caused by species such as hydrides can eliminated or corrected for. Measurements of small particles demand that high spatial resolution accompany the high mass resolution.

Refractory particles separated from primitive meteorites have been discovered to be of presolar origin [3] and have a wide range of isotopic compositions. These presolar particles are typically small ($\sim$1 μm or less) and can be minerals such as SiC and corundum. Isotopic perturbations of the Si in SiC from the Murchison meteorite range from enrichments of $\sim$20% in the minor isotopes to relative depletions of $\sim$60% [4]. The combination of small size and large range in isotopic composition make these particles good candidates for measurements by ToF–SIMS SIMS to demonstrate its capabilities and test its limits. In addition, increasing the spatial resolution with which these measurements are made may reveal other

* Corresponding author. E-mail: albert.fahey@nist.gov

PII S1387-3806(01)00435-3

features and inhomogeneities that have, as yet, not been observed in these meteoritic presolar particles.

2. ToF–SIMS versus magnetic-sector SIMS

Isotopic ratio measurements made with magnetic-sector SIMS instruments are typically performed by peak switching between the isotopes of an element and measuring the signal on a detector for a selected time interval for each isotope. The magnet is cycled through all of the isotopes multiple times as the signals for each isotope are measured one at a time. Automated peak centering and charge compensation can be performed at prescribed intervals and for selected isotopes. In addition, time information can be recorded during the measurement to remove secular variations in the signals (see, e.g., [5]).

When isotopic ratio measurements are made with ToF–SIMS, the entire spectrum is collected "in parallel" for a selected period of time. When ions arrive at the detector, they are counted and have their arrival times recorded. The data are then added into the appropriate channels in the spectrum. The primary concerns are both keeping the count rate for the isotopes of interest low enough so that the major isotope peaks are not saturated with dead-time losses and ensuring that the mass resolution is high enough to resolve interferences. Although variations in the signal may occur over the course of a measurement, the cyclic variations that are observed in magnetic sector instruments do not occur, because ions are generated randomly when the primary ion pulse hits the sample. Isotope ratio measurements in ToF–SIMS are more calculation than measurement, since the analysis is performed after the spectrum is acquired and no adjustments are made during the acquisition.

3. Experimental

The isotope ratio measurements reported here were made on a CAMECA (IonToF) ToF–SIMS IV[1] instrument equipped with a total of four ion sources. A high-current Ga^+ ion gun is typically used for analysis because of its high spatial resolution and short pulse duration. A dual-source column that can be used for both sputtering and analysis with either Cs^+ or an electron impact source in which we ran O_2^+ is also available. In addition, the instrument has a second electron impact source that can be used for analysis and an electron flood gun for charge compensation on insulating samples. The mass spectrometer is a linear reflectron-type spectrometer with a single microchannel plate and scintillator coupled to a photomultiplier tube for the ion detector. The ion detector is also equipped with post-acceleration variable up to 10 kV. A schematic of the instrument configuration is shown in Fig. 1. A secondary accelerating voltage of 2 kV and a post-acceleration of 10 kV were used for this study.

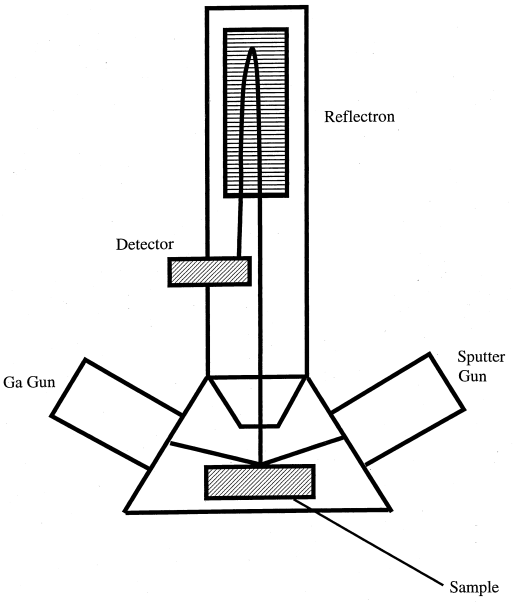

Fig. 1. A schematic diagram of the ToF–SIMS IV as used in this study. Two ion beams can be focused onto the sample. Ions are extracted above the sample into the linear time-of-flight mass spectrometer.

The Ga^+ ion gun can be operated in three different modes; however, only two of the modes are generally used. In the highest-current mode, known as the bunched-mode, all three lenses of the gun are ener-

[1] Certain commercial equipment, instruments, or materials are identified in this article to adequately specify the experimental procedure. Such identification does not imply recommendation or endorsement by the National Institute of Standards and Technology, nor does it imply that the materials or equipment identified are necessarily the best available for the purpose.

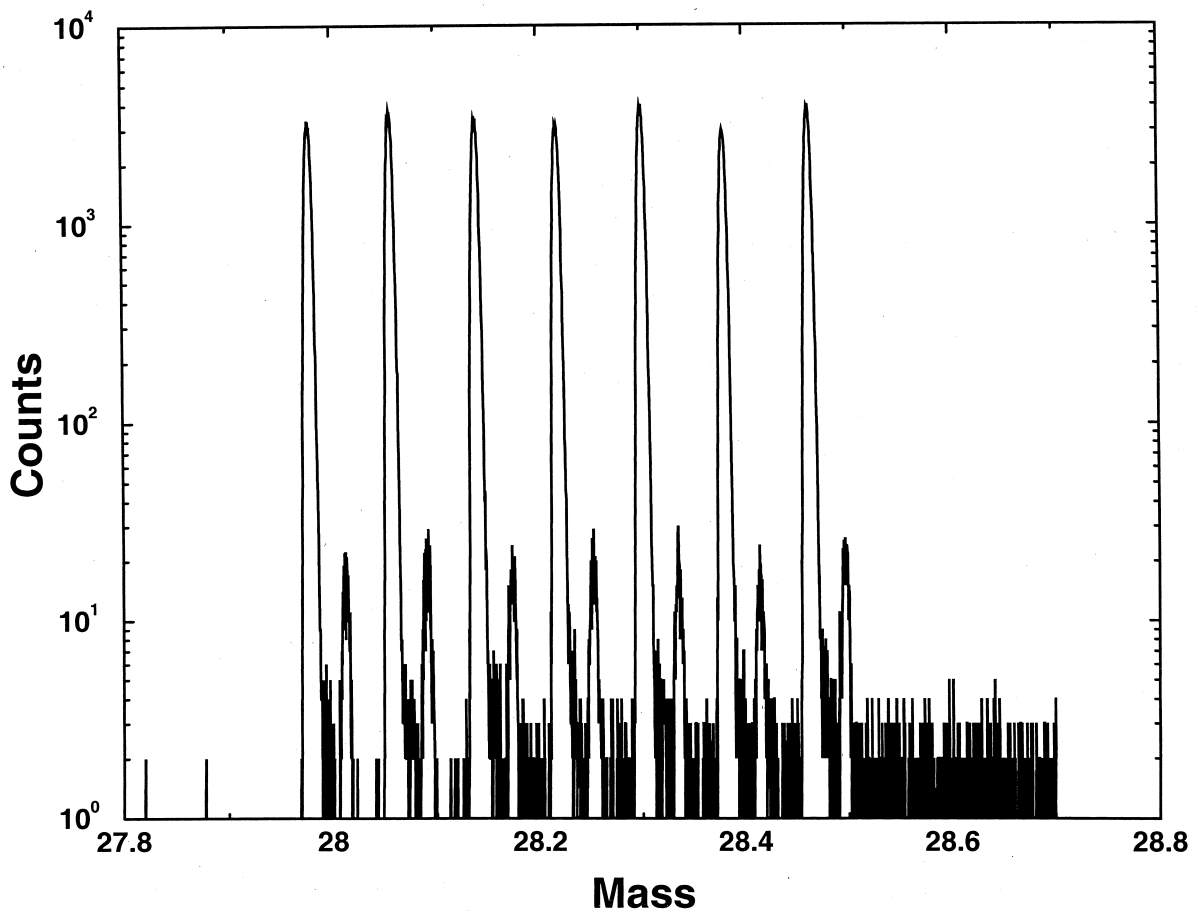

Fig. 2. Burst-mode mass spectrum in the region of ^{28}Si.

gized and the ion buncher is used to yield an ion pulse of ~0.7 ns duration and a spot size of ~2 μm. Higher spatial resolution can be achieved by using only two of the lenses in the gun in a mode known as burst mode, yielding a spot size of ~0.2 μm. Many fewer ions are in the ion pulses, since they are no longer bunched pulses, and they have ~1.2 ns duration. This would, in general, be a significant limitation for simultaneously achieving high spatial resolution and high mass resolution. However, the ToF–SIMS IV has a dual set of blanking plates that can be used to produce bursts of primary ion pulses. A plot of the peaks in the region of ^{28}Si generated by a burst-mode Ga^+ beam modulated at 20 MHz is shown in Fig. 2. The peaks are spaced ~250 channels (~25 ns) apart because of the 20-MHz modulation on the blanking plates, and there are seven peaks defined by the envelope of the rectangular unblanking pulse applied to the second set of plates. A mass-resolved image demonstrating the spatial resolution taken in this mode is shown in Fig. 3. The ^{28}Si image shows terrestrial SiC particles that are ~1 μm in diameter. All of the data for particles in this article was taken with a burst-mode Ga^+ primary beam. The Ga^+ beam was rastered over the sample with eight bits of resolution in the *x* and *y* directions for all of the data presented in this article.

Unlike dynamic SIMS, which occurs in magnetic

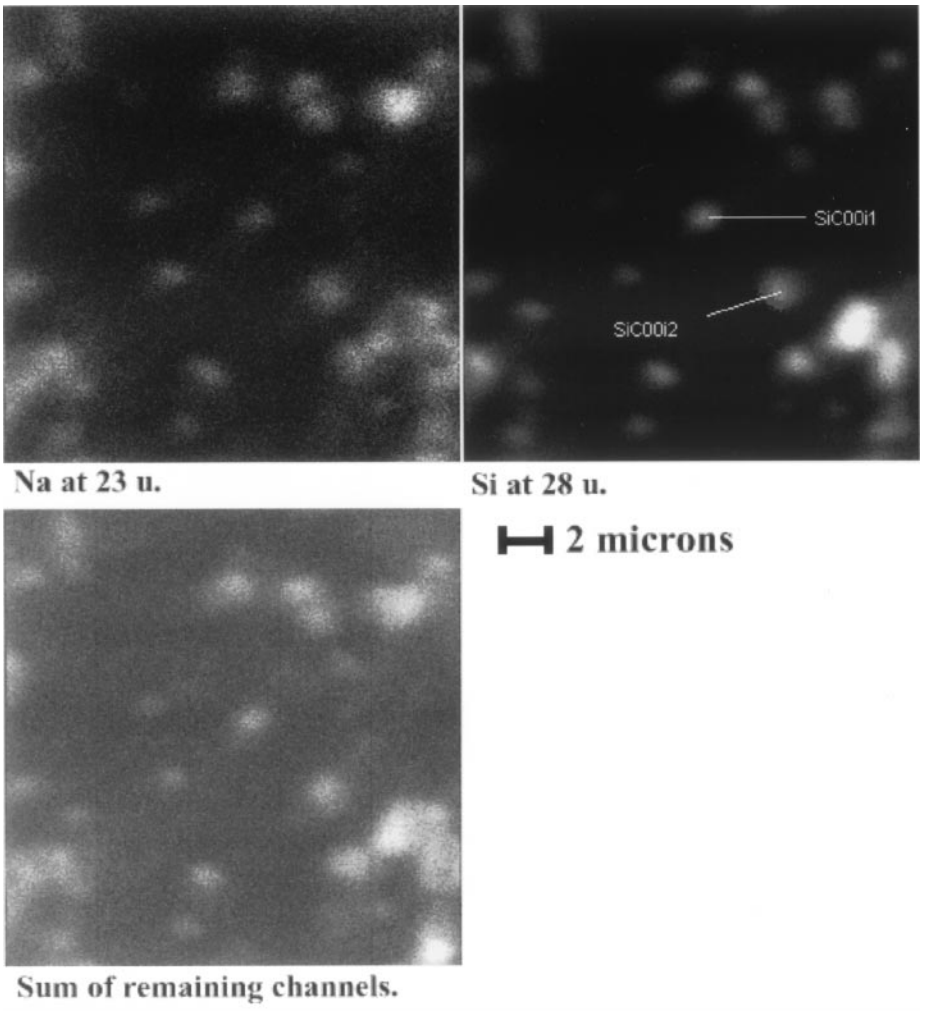

Fig. 3. Mass-resolved image of terrestrial SiC particles. Particles of 1–2 μm are visible, showing that the beam diameter is small enough to discern such features. The image is 256 × 256 pixels in size. The signals from the multiple peaks generated in the burst mode for each mass were summed to form the mass-resolved images shown.

sector instruments, the erosion rate of the surface in ToF–SIMS is very low, such that the deposition rate of species onto the surface from the vacuum is higher, for some species like H, than the sputter rate from the surface due to Ga^+ bombardment. This produces significant hydride peaks that can affect isotope ratio measurements significantly for most elements. Hydride production can be significantly reduced by sputtering the surface with a second ion beam. The ion beams are temporally interlaced during a single analysis cycle; a schematic of the timing is shown in Fig. 4. Typically, the repetition rate of the Ga^+ ion beam is 10 kHz, as it takes ~100 μs for most of the secondary ions to traverse the mass spectrometer. The duty cycle of the sputter beam can be varied to control the erosion rate of the material under analysis. The sputter beam used for measurement of positive secondary ions in this study was O_2^+ generated with the electron impact source. Fig. 5 shows a time profile for the peaks: ^{28} Si, ^{29}Si, and ^{28}SiH with and without O_2^+ sputtering and with the addition of O_2 flooding. One can see that the $^{28}SiH^+$ signal with sputtering is much

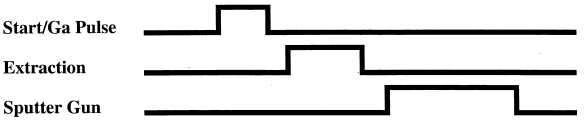

Fig. 4. Timing diagram illustrating the sequence of events during a single cycle of dual-beam ToF–SIMS analysis. Typically, the Ga beam is unblanked for 100–200 nsec. The duration of the on time of the sputter beam is variable but is typically most of the 100–120 μsec duration of the entire cycle.

lower than that without sputtering. In addition, the O_2 flooding provides an ion-yield enhancement for the Si. The data shown in Fig. 5 were taken by selecting a region of interest in the mass spectrum and plotting the data in that region over time. Since, for the purpose of this measurement, the regions were not carefully chosen to be uniform, an accurate isotope ratio cannot be expected from this data; however, the relative signals for ^{28}Si and ^{29}Si at the end of the profile are approximately correct. Although we have not directly measured the sputter rate, it is high enough so that the H background on the sample is reduced; however, we have not yet consumed an entire particle, even the smallest we have seen, during any analysis.

Minor sample charging did occur with the use of the electron-impact sputter source; however, the electron flood gun compensated for any charging. Charg-

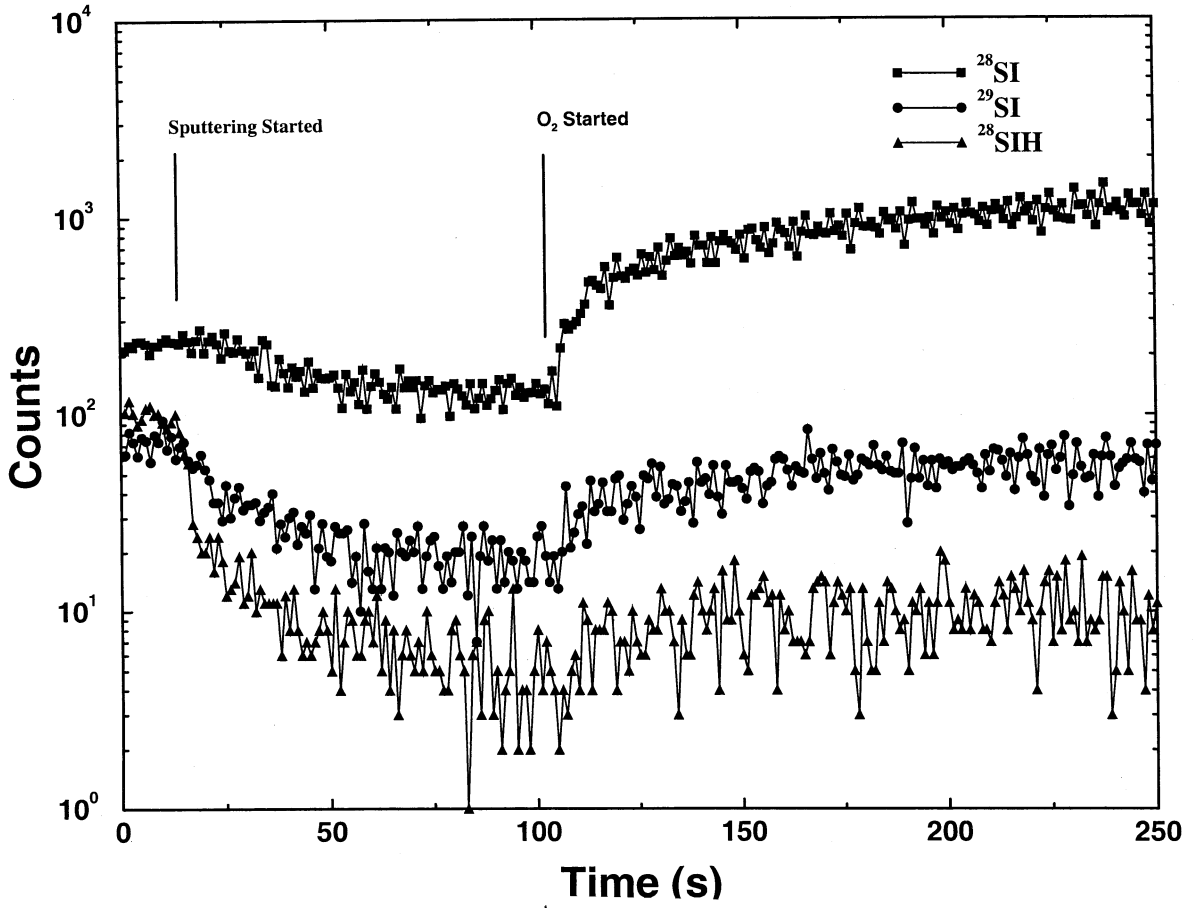

Fig. 5. Time profile showing the signals from ^{28}Si, ^{29}Si, and ^{28}SiH under three different experimental conditions. First, near the origin without O_2^+ sputtering or oxygen flooding the signal due to ^{28}SiH is larger than the ^{29}Si signal; second, once O_2^+ sputtering is added, the ^{28}SiH signal drops below the level of the ^{29}Si signal; and third, when O_2 flooding is added, the elemental signal increases.

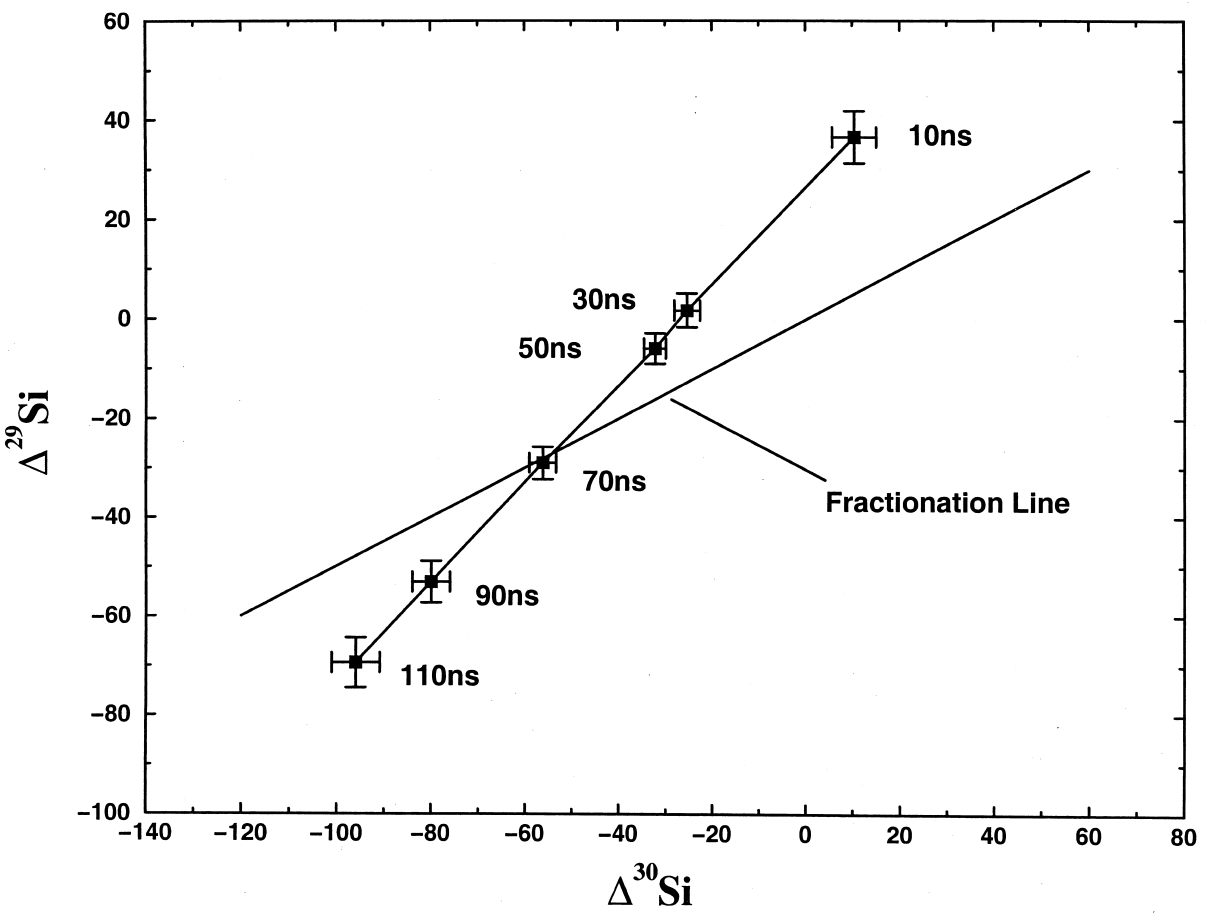

Fig. 6. Three isotope plot of Si isotopic measurements (where $\Delta^{i}X = ({}^{i}X/{}^{Ref}X)_{Meas.}/({}^{i}X/{}^{Ref}X)_{Std.} - 1] \times 1000$, and the reference isotope is ^{28}Si) shown with different values of dead time applied to the spectrum. Each point is a mean of the results from multiple spectra taken with similar count rates. Dead-time variations affect the position of the data by moving it along a line of unity slope, because the dead-time correction mainly effects the denominator, ^{28}Si, which is also the most abundant isotope. Other mass-dependent variations would move points along a line of slope 1/2.

ing on particles typically manifests itself in a visible, horizontal-intensity variation across the particle. It did not appear to significantly affect the measurement of the isotopic ratios, however. The electron flood gun was used for charge compensation for all of the measurements reported here.

A typical series of measurements begins with tuning and alignment of the instrument. This is facilitated by the reloading of setup files that record the previous state of the instrument and allow the operator to re-establish conditions at a later time. Once the ion guns are operating and all of the voltages have been applied, fine-tuning of the Ga^{+} gun focus can be achieved by observing a secondary electron image of a TEM grid, or of some other sample with fine features, with a fast primary beam raster. Collection of a mass spectrum from almost any surface yields sufficiently numerous peaks to perform a mass calibration and to check and adjust the secondary peak shape. Finally, the sputter gun and the Ga gun rasters can be aligned to be concentric by observing the image of the total ion signal and looking for the change in ion yield caused by the sputter gun ion beam.

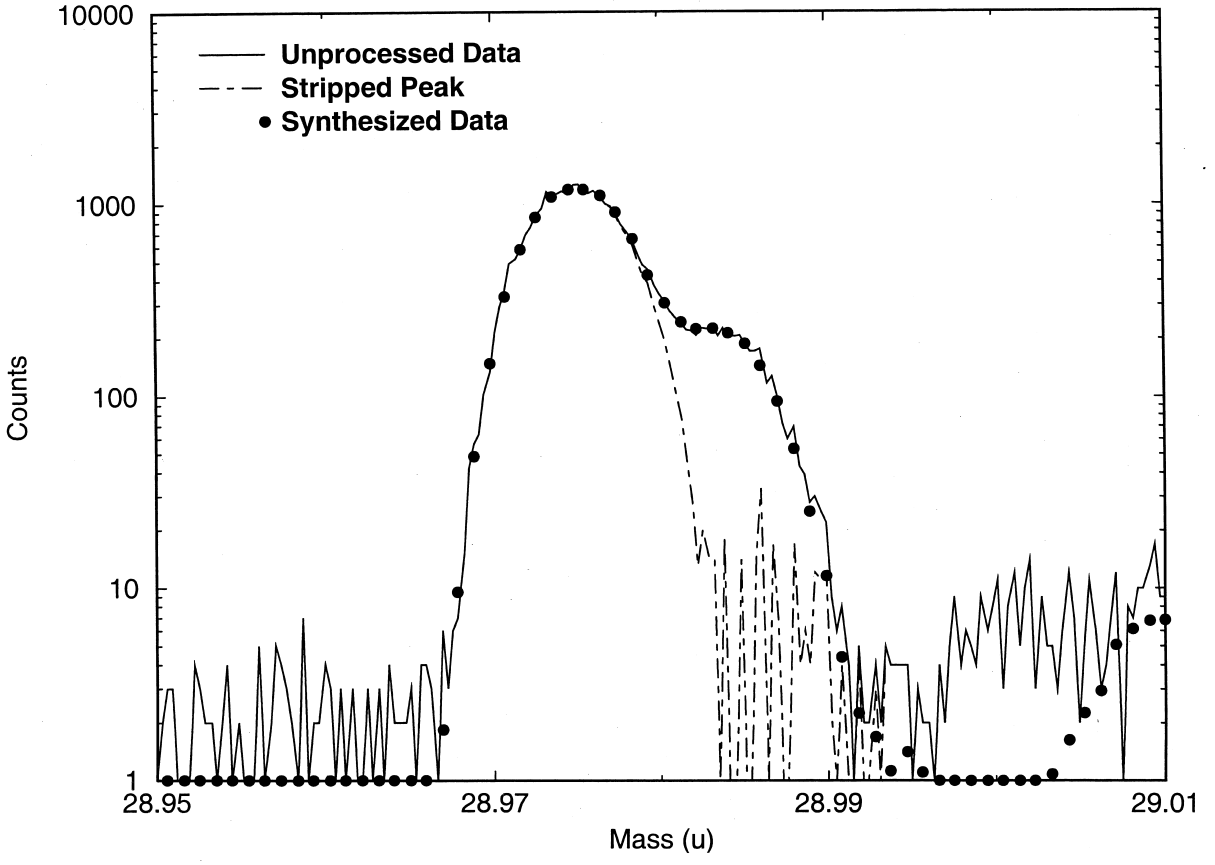

Fig. 7. A plot of the combined burst mode peak at the mass of ^{29}Si. The peak synthesized from the ^{28}Si peak is also shown, along with the ^{29}Si peak after the ^{28}SiH contribution has been stripped.

To locate particles, a spectrum of a material with the elements of interest is taken and the peaks of the major isotopes of interest are marked as regions of interest and put into a "peak list." An image at moderate magnification (typically 200 × 200 μm) of the mass ranges identified in the peak list is acquired, and a region where the particles of interest are found is selected for acquisition of a higher-magnification image. This process can be iterated until the particles of interest span enough pixels so that a subregion of the rastered area that encompasses only one particle can be selected for analysis by defining a "raster mask." The definition of a raster mask is a key tool for particle analysis, since the instrument can be set up to image a single region that contains multiple particles of interest and all of the particles in this region can be analyzed by simply defining a new raster mask for each particle—nothing else needs to be changed. In the images shown in Fig. 3, a 1-μm particle spans ~25 pixels. Raster masks were defined for two of the particles in this image, and spectra were acquired for 10 min on each of the particles.

4. Treatment of data

The specialized handling of the data required for isotope measurements demanded that we write our own software to analyze it. The algorithm needed for isotope ratio measurements can be divided into four

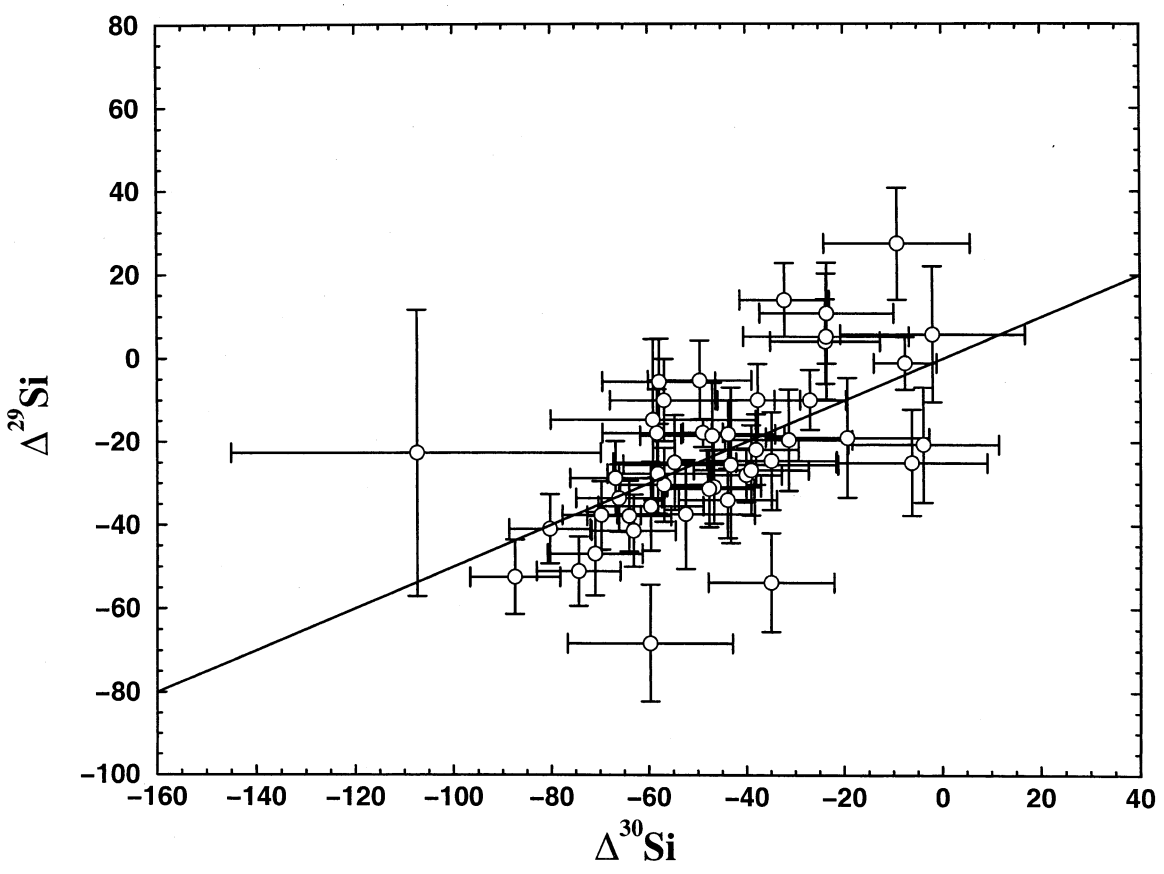

Fig. 8. A three-isotope plot of the composition of terrestrial SiC shows that the data cluster around the mass fractionation line and fit a line whose slope is nearly 1/2, as expected.

"custom" tasks. First, a dead-time correction had to be applied, but, also, the dead time (τ) had to be determined. The best way to determine the dead time is to make an isotope ratio measurement [6]; hence, the process was forced to be an iterative one. Second, proper peak location and identification is important if one wants the program to run automatically with the ability to process many data files in an unattended manner. Fortunately, the mass calibration in our ToF–SIMS is of adequate quality to allow the use of known exact masses for peak location. Because the spectra for high spatial resolution ToF–SIMS are taken in burst mode, accompanying the process of peak location is the location of all of the burst-mode peaks for a given isotope. Third, once peaks are located, those that have interferences, such as $^{28}SiH^+$ with $^{29}Si^+$, must be fitted and the interference signal subtracted. Finally, the peaks can be integrated and the ratios formed.

The details of the dead-time correction for ToF–SIMS have been discussed previously [2]. The ToF–SIMS IV instrument is equipped with a multistop time-to-digital converter (MSTDC). Thus, the equations that apply to the dead-time correction of the data presented here are

$$I_{\mathrm{cor}}^{(c)} = -N\ln\left[1 - \frac{I_{\mathrm{exp}}^{(c)}}{N'(c)}\right] \tag{1}$$

and

$$N'(c) = N - \sum_{c'=c-c_\tau}^{c-l'} I_{\mathrm{exp}}^{(c)}, \tag{2}$$

Table 1
Isotopic measurement of synthetic SiC[a]

Sample	Δ^{29}Si	σ	Δ^{30}Si	σ	δ^{30}Si	σ	r_{29}	r_{30}
a	−20.7	13.9	−3.9	15.3	37.5	31.7	1.2	1.0
b	5.8	16.2	−2.0	18.8	−13.6	37.4	1.1	1.1
c	−28.1	6.5	−40.1	7.3	16.2	14.9	1.3	1.2
d	−1.1	6.3	−7.6	6.4	−5.4	14.1	1.7	1.4
e	−9.9	7.2	−27.0	7.3	−7.2	16.1	1.4	1.2
f	−9.9	7.2	−27.0	7.3	−7.2	16.1	1.4	1.2
g	−18.2	8.2	−43.8	9.6	−7.5	19.0	1.2	1.2
h	−25.0	12.8	−6.3	15.4	43.8	29.9	1.1	1.1
i	−26.9	10.9	−39.1	11.8	14.7	24.7	1.4	1.2
j	−52.5	8.9	−87.5	9.2	17.4	20.1	1.8	1.6
k	−46.9	10.0	−71.1	9.7	22.6	22.3	1.7	1.3
l	−14.8	19.4	−59.2	21.0	−29.5	44.1	1.2	1.1
m	−37.5	13.1	−52.5	14.1	22.5	29.8	1.3	1.2
n	−35.5	10.7	−59.7	10.8	11.2	24.0	1.4	1.2
o	−41.0	8.3	−80.4	8.3	1.5	18.5	1.7	1.5
p	−9.9	8.6	−37.7	8.7	−18.0	19.3	1.7	1.5
q	−33.6	8.1	−66.2	8.8	1.0	18.5	1.8	1.7
r	4.1	10.1	−23.9	11.2	−32.2	23.1	1.2	1.2
s	−37.7	8.2	−69.8	8.0	5.6	18.2	2.1	1.7
t	10.8	12.0	−23.6	13.7	−45.2	27.7	1.2	1.2
u	−51.1	8.3	−74.5	8.6	27.7	18.8	2.0	1.8
v	−68.3	14.0	−59.8	16.9	76.8	32.7	1.1	1.1
w	−28.8	8.9	−66.9	9.3	−9.3	20.0	2.1	1.9
x	−25.0	11.4	−4.8	12.6	−4.8	26.1	1.3	1.2
y	14.0	8.7	−32.2	9.2	−60.3	19.7	1.8	1.7
z	−53.8	11.8	−35.0	12.9	72.6	27.0	1.3	1.2
α	−19.6	12.2	−31.4	13.0	7.8	27.6	1.2	1.1
β	−5.2	9.5	−49.6	10.6	−39.2	21.8	1.2	1.2
χ	−17.9	3.4	−49.0	4.1	−13.1	8.0	ND	ND
δ	−30.9	8.8	−46.7	9.6	15.2	20.1	1.3	1.3
ϵ	−18.0	10.6	−58.4	11.2	−22.4	24.0	1.2	1.1
ϕ	−10.0	9.9	−57.0	11.0	−37.1	22.6	1.2	1.2
γ	−18.6	12.8	−47.1	14.8	−9.9	29.5	1.1	1.1
η	−5.5	10.2	−58.0	11.6	−47.0	23.5	1.2	1.1
ι	5.3	15.0	−23.7	16.9	−34.3	34.4	1.1	1.1
φ	−31.4	9.2	−47.7	9.2	15.2	20.6	1.5	1.2
κ	−22.7	34.4	−107.5	37.6	−62.0	78.3	1.1	1.1
λ	−30.4	8.9	−57.0	9.0	3.9	19.9	1.8	1.5
μ	−19.0	14.4	−19.4	16.7	18.6	33.3	1.1	1.1
ν	−24.6	11.8	−34.9	13.3	14.2	27.0	1.2	1.1
o	−27.7	9.6	−58.2	10.4	−2.8	21.8	1.4	1.3
π	−25.6	18.7	−43.3	22.0	7.8	43.4	1.1	1.1
θ	27.4	13.3	−9.2	14.9	−64.1	30.4	1.2	1.1
ρ	−21.9	8.5	−38.1	8.7	5.8	19.1	1.6	1.4
σ	−41.4	8.6	−63.2	8.6	19.5	19.3	1.8	1.5
τ	−37.9	8.5	−64.1	8.6	11.7	19.1	1.6	1.4
υ	−34.0	9.2	−43.9	10.1	24.1	21.0	1.3	1.2
All samples	−22.3	1.3	−47.1	1.4	−1.9	3.0		
χ^2		3.4		4.1		1.4		

[a] ND—Not determined. Δ—Delta value in permil not corrected for mass bias. σ—1 σ uncertainty. r_{xx}—Ratio of the assigned uncertainty to the uncertainty caused by counting statistics. δ—Delta value in permil corrected for mass bias with an internal correction.

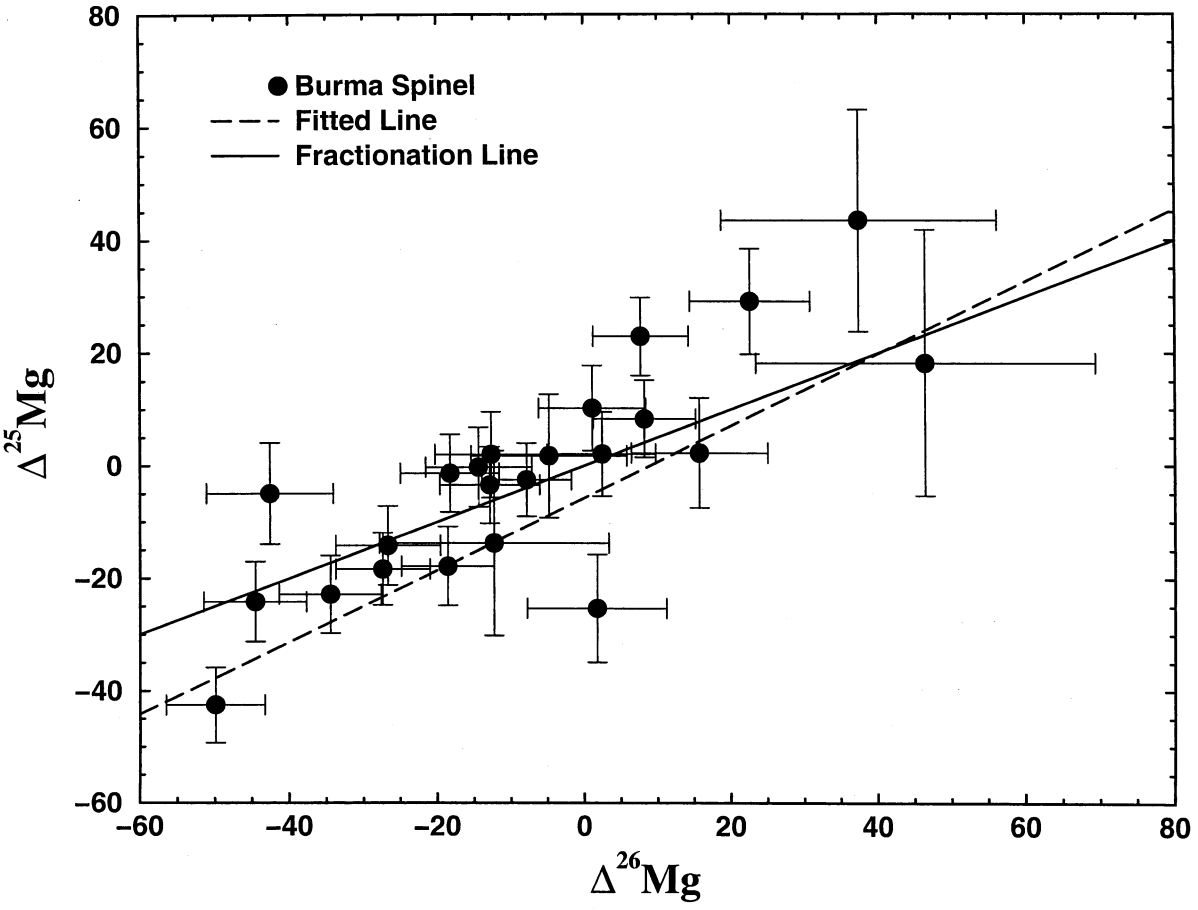

Fig. 9. A three-isotope plot of the Burma spinel composition shows that the data lie along the terrestrial mass fractionation line.

where c is the channel number, c_τ is the number of channels that span the dead time period (i.e., (2) $c_\tau = \tau/\tau_{res}$ with τ_{res} being the time resolution of the MSTDC), $I^{(c)}_{exp}$ is the experimentally measured intensity, or counts, in channel c, $I^{(c)}_{cor}$ is the corrected counts in channel c, and N is the number of primary beam pulses during the measurement. The dead-time correction was applied to the entire spectrum for the data reported here. This is somewhat inefficient, as the dead-time correction is the longest part of the calculation and only a small region of the spectrum is being examined. The effect of the dead-time correction on the Si isotope ratio measurements is shown in Fig. 6. Each point in Fig. 6 is an average of a set of measurements taken with similar count rates. One can see that the regression line though the data passes through the mass-fractionation line at a dead time of 70 ns. In addition, the mass-fractionation value on which the 70-ns point lies is similar to that typically measured by dynamic SIMS. A dead time of 70 ns means that several peaks in a burst-mode spectrum influence each other because the burst-mode peaks are only separated by ~25 ns.

The method used for peak identification was very simple. The lowest-mass, most intense peak in the region of the exact mass of the isotope was identified as the sought-after peak. This was true for all of our data. The number of burst-mode peaks is stored in the data file. However, the burst-mode peaks are not perfectly spaced; therefore, the center-of-mass of each

Table 2
Mg isotopic composition of terrestrial Burma Spinel[a]

Sample	Δ^{25}Mg	σ	^{26}Mg	σ	δ^{26}Mg	σ	r_{25}	r_{26}
A	–22.8	6.9	–34.5	6.9	11.0	37.2	2.2	2.3
B	−4.9	9.0	−42.6	8.5	−32.9	46.3	1.3	1.3
C	1.8	11.0	−4.8	10.6	−8.4	22.4	1.2	1.2
D	−13.7	16.4	−12.3	15.6	15.2	35.1	1.1	1.1
E	8.4	6.9	8.2	7.0	−8.5	16.1	1.7	1.8
F	−3.4	6.8	−12.9	6.8	−6.2	18.7	2.2	2.3
G	−0.2	7.1	−14.4	7.2	−13.9	20.2	2.3	2.5
H	−14.1	7.0	−26.7	7.1	1.6	30.1	2.2	2.3
I	10.3	7.6	1.1	7.3	−19.4	15.2	2.0	2.0
J	−2.5	6.5	−7.9	6.1	−3.0	15.3	2.2	2.1
K	−18.3	6.4	−27.4	6.4	9.1	30.3	2.2	2.3
L	−1.3	6.9	−18.3	6.7	−15.7	23.0	2.3	2.3
M	2.1	7.5	2.4	7.3	−1.8	15.1	1.6	1.6
N	2.3	9.8	15.7	9.3	11.1	25.1	1.4	1.3
O	29.2	9.3	22.6	8.2	−35.8	29.2	1.6	1.4
P	−25.3	9.6	1.7	9.5	52.3	19.3	1.2	1.2
Q	18.3	23.6	46.4	23.0	9.9	66.2	1.0	1.0
R	43.5	19.6	37.4	18.7	−49.6	54.2	1.1	1.0
S	−17.8	7.0	−18.6	6.3	17.1	23.3	2.2	1.9
T	23.0	6.9	7.7	6.5	−38.3	15.9	1.7	1.7
U	2.0	7.6	−12.7	7.6	−16.7	19.8	1.6	1.7
V	−42.5	6.7	−49.9	6.6	35.2	51.6	2.2	2.3
W	−24.1	7.1	−44.6	6.9	3.5	46.8	1.9	1.9
All Samples	−5.7	1.6	−13.8	1.6	−5.9	4.7		
χ^2		4.9		7.2		0.9		

[a] Δ—Delta value in permil not corrected for mass bias. σ—1 σ uncertainty. r_{xx}—Ratio of the assigned uncertainty to the uncertainty due to counting statistics. δ—Delta value in permil corrected for mass bias with an internal correction.

burst-mode peak was used to determine the peak position. All of the burst-mode peaks for each isotope were then summed, with the appropriate overlapping centroids, to produce a composite peak.

Some elements like Si, Mg, and Ti usually have significant interferences at the minor isotopes caused by hydrides of a major isotope. Signals for the hydrid were subtracted from the minor isotopes by fitting the data at the minor isotope to the scaled and shifted peak data of the major isotope. Fig. 7 shows a plot of the data from a terrestrial SiC particle and the fitted peaks of the ^{29}Si and the ^{28}SiH derived from the ^{28}Si peak. The data from the ^{28}Si peak are fitted to the ^{29}Si and the ^{28}SiH data by minimizing the expression

$$\chi^2 = \sum (S_m^i - Ax_i - By_i)^2, \quad (3)$$

where i spans the region around the peak to be corrected, S_m^i is the measured spectral data in the region of interest, x_i is the major isotope data (e.g., ^{28}Si) shifted to the position of the isotope data to be fitted, and y_i is the major isotope data shifted to the position of the hydride interference. In practice, the isotope data to be fitted (e.g., ^{29}Si) is assumed to be more intense than the interfering peak; thus, its center is easily identified. The interference peak position is then referenced from the center of the peak to be corrected, thus ensuring accurate positioning of the shifted data from the major isotope.

The solution to Eq. (3) is

$$B = \frac{\sum S_m^i x_i \sum x_i y_i - \sum S_m^i y_i \sum x_i^2}{(\sum x_i y_i)^2 - \sum x_i^2 \sum y_i^2}; \quad (4)$$

$$A = \frac{\sum S_m^i y_i \sum x_i y_i - \sum S_m^i x_i \sum y_i^2}{(\sum x_i y_i)^2 - \sum x_i^2 \sum y_i^2}. \quad (5)$$

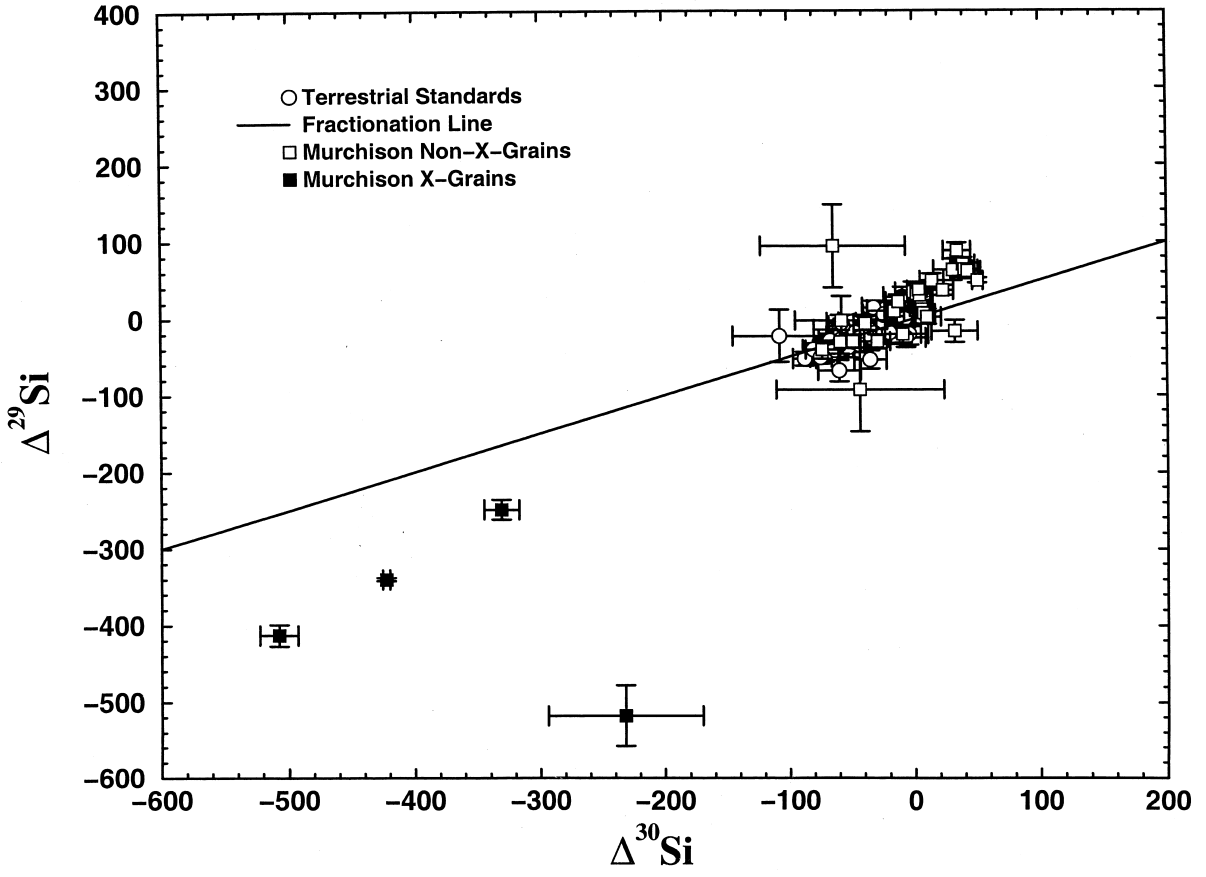

Fig. 10. A three-isotope plot of all of the Si isotopic data taken show that most of the Murchison meteorite data cluster near the origin but appear to lie on a line of slope somewhat larger than 1/2. In addition, four grains have significant relative enrichments of ^{28}Si.

Once A and B are computed, the hydride contribution, By_i, is subtracted from S^i_m. The peaks are then integrated to the 10% level. If a minor isotope peak has less than 20 counts at its maximum, then a fixed width computed from the major isotope is used for the integration.

5. Peak integration and sources of uncertainty

The corrected composite data used to form the ratios for the isotopes has three potential contributing sources of uncertainty. First, an interference correction could have been applied incorrectly. This type of error can be checked by noting that the width of the corrected peak is not significantly different than that of other peaks that have not had a correction applied. An error of this kind is a systematic error and is not accounted for during data analysis. The other sources of uncertainty are counting statistical variation, which can easily be calculated, and the uncertainty in the integration of the peaks caused by binning. The latter uncertainty arises when a relatively small number of channels are used for the integration. Typically, the 10% width of peaks in the region of Si was 30–50 channels (variance of ~40 (channels)^2). This implies that addition or omission of one channel at the 10% edge could affect the integral of the peak by more than counting statistical uncertainties alone would predict. Therefore, this additional component of the uncertainty was added to the total computed uncertainty.

The binning uncertainty was approximated by the mean intensity of the low-mass and high-mass 10% cutoff channels. The binning uncertainty is compounded with the counting statistical error into the total uncertainty for the integral. The ratio of the total uncertainty to that due to counting statistics is typically 1 to 2 for the Si isotopes measurements reported here.

6. Isotope ratio data

Isotope ratios were measured in particles of SiC (Alfa AESAR Stock 40155) and $MgAl_2O_4$ (Burma Spinel USNM B12071) as well as a several SiC particles from the Murchison meteorite. All of the particles were less than ~2 μm in size. None of the particles was completely consumed in the analyses presented here.

The isotope data are reported in "delta-value" notation, which is the parts-per-thousand deviation from the terrestrial (or standard) ratio (i.e., $\Delta^{i}X = [(^{i}X/^{Ref}X)_{Meas.}/(^{i}X/^{Ref}X)_{Std.} - 1] \times 1000$). The upper-case delta ($\Delta^{i}X$) indicates a delta value that has not been adjusted for any kind of mass fractionation. A lower-case delta value ($\delta^{i}X$) means that a mass fractionation correction has been applied. In this work, only internal linear mass fractionation corrections have been made. An internal linear mass fractionation correction is made by choosing one of the measured isotope ratios and assuming that the deviation of that measured ratio from the standard ratio is only attributable to a fractionation that depends linearly on mass. The mass fractionation can thus be computed and applied to the other isotopes of the element measured.

6.1. Si isotopes

A three-isotope plot of the measurements made on synthetic SiC particles is shown in Fig. 8. An unweighted fit of the data to a line gives a slope of 0.56 ± 0.08, consistent with the expected mass fractionation line of slope 1/2. The intercept is 4.6 ± 4.5, consistent with the origin, as expected. A weighted fit of the data gives a line of slope 0.53 ± 0.03 ($\chi^2_\nu = 1.4$) when the fit is forced through the origin. If the fit is not forced through the origin, then the weighted fit does not give sensible results, since the range of values is not very large. This can be seen from Table 1, because the weighted means of Δ^{29}Si and Δ^{30}Si have χ^2_ν, values of 3.4 and 4.1, respectively. One expects that the Δ^{29}Si and Δ^{30}Si values should scatter more than the individual uncertainties might imply since variations in the instrumentally induced mass bias are not accounted for in the individual uncertainties. With the given χ^2_ν values in Table 1, the Δ^{29}Si and Δ^{30}Si scatter at a level of only approximately twice the assigned uncertainty. The data for the δ^{30}Si, which is internally corrected for mass bias, gives a mean value of -1.9 ± 3.0 with a $\chi^2_\nu = 1.4$, consistent with data taken from a single population.

The last two columns in Table 1 show the ratio of the assigned uncertainty of each delta value to the counting statistical uncertainty. These ratios deviate from unity because of the compounded uncertainty caused by the binning of the data by the TDC. Although many of these values are near unity, some are larger than 2, showing that the uncertainty induced by binning can be significant.

6.2. Mg isotopes

A three-isotope plot of the measured Mg isotope ratios is shown in Fig. 9. The data fit a line of slope 0.6 ± 0.1, which is consistent with the expected slope 1/2 mass fractionation line, with an intercept of -5.7 ± 4.7. Table 2 shows the individual delta values for the Mg isotopes measured in Burma spinel. The values of $\chi^2_\nu = 4.9$ and 7.2 for the mean values of the Δ^{25}Mg and Δ^{26}Mg, respectively, show that the mass fractionation does not vary a great deal but does vary more for Mg than for Si. The mass fractionation–corrected δ^{26}Mg values have a mean value consistent with zero at 1.3 σ. The χ^2_ν value for δ^{26}Mg shows that the data scatter is consistent with a normal distribution.

6.3. Meteorite data

Silicon carbide grains from the Murchison KJG acid residue [7] were measured for their Si and Mg isotopes. The grains were dispersed on sputter-cleaned gold foil pressed into the surface of an SEM

Table 3
Isotopic compositions of Murchison X grains[a]

Sample	Δ^{30}Si	σ	Δ^{29}Si	σ	Δ^{26}Mg	σ	$(^{26}Al/^{27}Al)_0$	σ
msc02b2b	−232	62	−518	40	11719	543	0.32	0.03
msc001c7	−508	15	−413	14	202072	11849	0.18	0.02
msc001c6	−423	3	−340	2	39599	303	0.21	0.02
msc04e1b	−331	14	−249	13	198268	7551	0.34	0.03

Δ—Delta value in permil not corrected for mass bias. σ—1 σ uncertainty. $(^{26}Al/^{27}Al)_0$—inferred initial ratio by assuming $(^{26}Mg/^{24}Mg)_{initial}$ is terrestrial.

stub. Individual grains were selected for analysis by imaging in ^{23}Na, ^{24}Mg, ^{26}Mg, ^{27}Al, and ^{28}Si, selecting regions that showed Si signals but not Na, ^{24}Mg, or Al. Individual grains with high ^{26}Mg signals and corresponding Si signals were always measured because of the possibility of the ^{26}Mg signal being attributable to the decay of ^{26}Al. Once a grain was identified, a spectrum from that grain was acquired by defining a raster mask for that grain and collecting data for 10 min. A raster mask causes the beam to be directed only to the points specified in the mask, thus producing a spectrum only from the region of interest in the image. Fig. 10 shows all of the Si isotope data. Both the terrestrial SiC and the meteoritic SiC data are plotted. The terrestrial slope 1/2 mass fractionation line is also drawn in Fig. 10. The meteoritic and terrestrial data tend to cluster around the origin, except for four, meteoritic grains, whose Si isotopic composition shows a high relative depletion of ^{29}Si and ^{30}Si.

Table 4
Si isotopic composition of non-X-grain Murchison SiC[a]

Δ^{29}Si	σ	Δ^{30}Si	σ
−40.6	11.8	−73.6	13.0
93.7	53.8	−64.6	57.9
−30.6	15.4	−59.1	16.3
−2.4	31.4	−58.0	36.8
−30.0	8.8	−49.0	9.3
−93.3	54.8	−43.3	67.0
−6.2	9.1	−39.1	9.2
−30.1	9.2	−29.4	10.4
10.0	17.8	−16.0	21.1
9.4	6.5	−15.7	7.9
21.5	9.4	−12.7	9.6
−20.3	11.7	−8.9	14.3
34.5	12.9	−0.7	14.2
31.7	4.2	2.0	5.0
36.7	8.8	3.8	9.3
22.2	9.2	4.6	9.4
14.8	8.8	6.0	9.1
11.7	5.5	6.1	6.6
6.8	5.3	7.7	6.5
2.2	9.8	10.4	11.0
48.9	9.1	14.2	9.4
36.7	6.7	23.1	8.1
63.0	13.8	31.1	15.5
−16.5	14.6	32.2	18.3
88.0	10.1	34.2	10.8
69.9	8.8	39.0	9.5
63.4	9.9	39.9	10.9
61.7	10.0	42.7	10.3
49.3	3.4	50.7	4.1

[a] Δ—Delta value in permil not corrected for mass bias. σ—1 σ uncertainty.

These four grains are typically called X grains and are postulated to have supernova origins. The data for the X grains are shown in Table 3. Values for the equivalent initial $(^{26}Al/^{27}Al)$ are given along with the Si and ^{26}Mg delta values. The initial $(^{26}Al/^{27}Al)$ value was computed by taking the ratio of the ^{26}Mg counts and the ^{27}Al counts measured on each grain and applying a sensitivity factor of 1.38 ± 0.12. This sensitivity factor was determined from the measurements of the Burma spinel and is similar to sensitivities measured on the ims-3f [8].

The remainder of the meteoritic data have net positive Δ^{29}Si and Δ^{30}Si values of 26.0 ± 1.5 permil and 9.6 ± 1.7 permil, respectively. A weighted fit to the data gives a slope of 0.98 ± 0.08 ($\chi^2_\nu = 2.2$). Most SiC grains (non-X grains) from the Murchison meteorite show positive Δ^{29}Si and Δ^{30}Si values and plot along a line of slope 1.34 [4]. The measured slope of the limited data set presented here is larger than that of the mass fractionation line but less than 1.34. It is not inconceivable that if enough particles were measured, as in other works, a slope of 1.34 would be

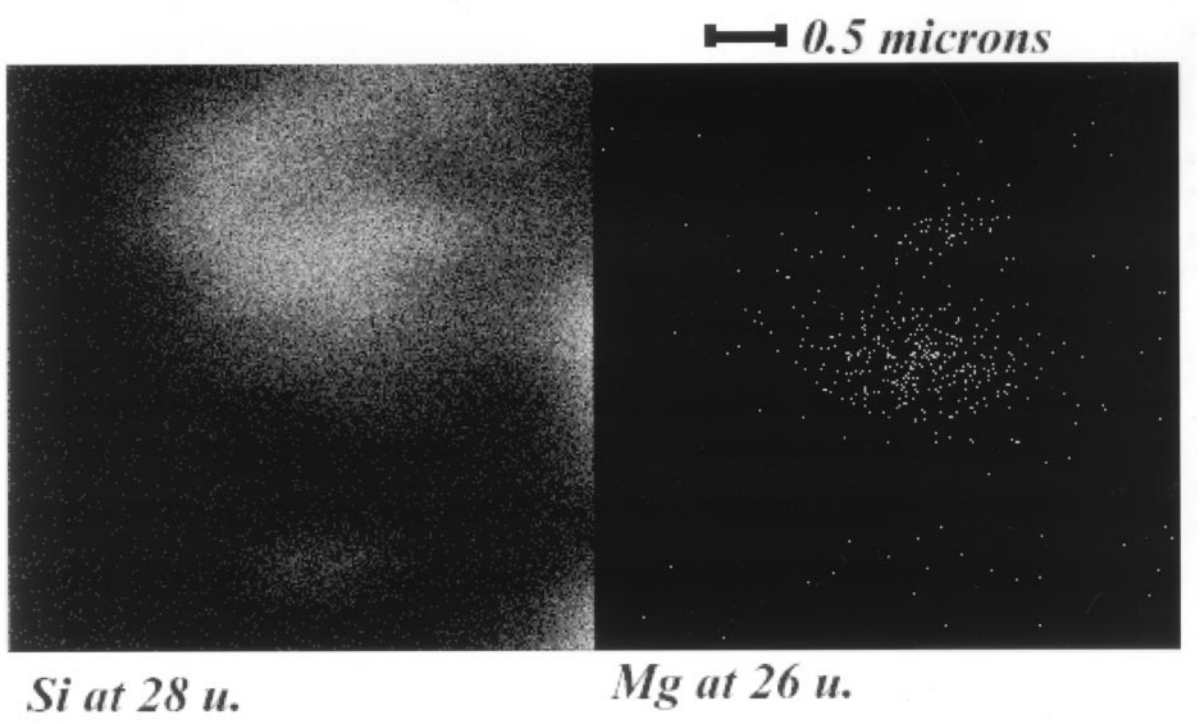

Fig. 11. Mass-resolved images near the Murchison X grain msc04e1 and the mainstream grain msc04e2 show that the two grains are apparently in intimate contact and are ~1 μm in size. The ^{26}Mg signal from the X grain msc04e1 appears to be coming from a shadowed area in the image; this is consistent with the data shown in Table 5.

Table 5
Isotopic composition of adjacent SiC grains from Murchison[a]

	Al counts	σ	^{27}Al/^{24}Mg ratio	σ	$(^{26}Al/^{27}Al)_0$ ratio	σ
msc04e1	138248	557	66.9	0.3	0.2420	0.0079
msc04e2	171302	720	45.2	0.2	0.0067	0.0006

	^{24}Mg counts	σ	^{25}Mg counts	σ	Δ	σ	^{26}Mg counts	σ	Δ	σ
msc04e1	2685	56	ND	ND	ND	ND	30862	223	116282	3807
msc04e2	4931	76	ND	ND	ND	ND	1783	43	2169	201

	^{28}Si counts	σ	^{29}Si counts	σ	Δ	σ	^{30}Si counts	σ	Δ	σ
msc04e1	203777.0	885.5	7871.0	97.2	-234.1	10.2	4715.0	71.6	-306.9	11.1
msc04e2	1514214.0	97.2	77496.0	71.6	8.5	6.6	51289.0	747.1	8.2	7.1

[a] ND—Not determined because of low signal level. Δ—Delta value in permil not corrected for mass bias. σ—1σ uncertainty. $(^{26}Al/^{27}Al)$—Inferred initial ratio by assuming $(^{26}Mg/^{24}Mg)_{initial}$ is terrestrial.

observed. The data for the non-X grains from Murchison are given in Table 4.

The high spatial resolution of the ToF–SIMS coupled with its ability to measure isotope ratios is demonstrated by the measurement of the Murchison X grain; msc04e1. Fig. 11 shows this particle along the adjacent particles on the mount. Particle msc04e1 apparently is directly adjacent to another particle, msc04e2, that was measured to have a mainstream Si isotopic composition. Table 5 gives the compositions of the two adjacent 1-μm particles. The two compositions are quite different, particularly for the Mg isotopes. With further work, we may be able to distinguish even smaller regions of isotopically anomalous material.

7. Conclusions

Isotopic ratio measurements have been made of small particles with a precision near that of counting statistics and a reproducibility comparable to dynamic SIMS measurements. The ToF–SIMS provides high spatial resolution and the ability to make precise measurements while consuming a small amount of the material analyzed.

Though making proper isotopic ratio measurements with a ToF–SIMS is not as simple as just using the vendor-supplied software, the implementation of a simple peak-finding and -stripping algorithm allows the measurements to be made correctly. The algorithm implemented in this work is specific to the elements and situations at hand; however, a more general identification and correction procedure may be developed that will be applicable to other elements, as well.

Acknowledgements

The careful work and helpful comments of two anonymous reviewers made this article better and accessible to a wider audience. Robert Vocke, Sonya Roberson, and David Simons of NIST made many useful suggestions regarding the details of this manuscript that strengthened its technical presentation.

References

[1] Z. Ma, R.N. Thompson, K.R. Lykke, M.J. Pellin, A.M. Davis, Rev. Sci. Instrum. 66 (1995) 3168.
[2] T. Stephan, J. Zehnpfenning, A. Benninghoven, J. Vac. Sci. Technol. A 12 (1994) 405.
[3] E. Zinner, in Astrophysical Implications of the Laboratory Study of Presolar Material, T. Bernatowicz, E. Zinner (Eds.), AIP, (1996) 3.
[4] P. Hoppe, I. Ott, in Astrophysical Implications of the Laboratory Study of Presolar Material, T. Bernatowicz, E. Zinner (Eds.), Woodbury, NY: AIP, (1996) 27.
[5] T.R. Ireland, Adv. Anal. Geochem. 2 (1995) 1.
[6] A.J. Fahey, Rev. Sci. Instrum. 69 (1998) 1282.
[7] S. Amari, R.S. Lewis, E. Anders, Geochim. Cosmochim. Acta 58 (1994) 459.
[8] A.J. Fahey, E.K.Zinner, G. Crozaz, A.S. Kornacki, Geochim. Cosmochim. Acta 51 (1987) 3215.